PAPER

Understanding ion diffusion in anion exchange membranes; effects of morphology and mobility of pendant cationic groups†

Mohammad Rezayani,[a] Farhad Sharif [ID] *[a] and Hesam Makki [ID] *[ab]

Anion exchange membranes (AEMs) are a promising low-cost alternative to cation exchange membranes (CEMs) in fuel cells. Among them, poly(2,6-dimethyl-1,4-phenylene oxide) with pendant quaternary ammonium (PPO-QA) is one of the most promising. PPO-QA membranes with flexible alkyl side-chains of varying lengths as a spacer (or extender) for QA have been studied and shown to have different performances; however, the exact underlying mechanisms have remained unclear. We study PPO-QA membranes with varying alkyl side-chains ($n = 0$, 6, 10, and 16 carbon atoms) with a constant QA position (near the backbone), and with the same side-chain length ($n = 16$) and varying QA positions on it: near the polymer backbone, in the middle, and at the end of the pendant side-chain, by molecular dynamics (MD) simulations. The calculated water diffusion coefficient in the membranes is in full agreement with experimental data. Our study on membranes with varying alkyl side-chain lengths and a constant QA position at different hydration levels shows a consistent and quantitative correlation between the anion diffusion coefficient (D_a) and the hydrophilic pathway morphology. Also, at constant hydration, D_a is considerably enhanced due to moving the QA position towards the end of the alkyl side-chain. However, we show that this enhancement is not due to morphological changes in the hydrophilic pathway or polymer phase. Still, the underlying mechanism is the enhanced mobility of QA, plus a lower residence time of anions close to QA. We show that the morphology of the membrane and the degree of phase separation between the hydrophobic/hydrophilic parts is almost constant, but the QA at the end of the alkyl side-chain is considerably easier to pull towards the water channels; therefore, its increased mobility and hydration result in the enhanced dynamics of the diffusing anion. Lastly, we introduce a new methodology to assess the correlation between membrane structure and ion transport rate for fuel cell membranes so that one can tune the permeation of ions (or other molecules) by two distinct mechanisms: (i) by controlling the hydrophilic pathway morphology by changing the polymer backbone structure, which determines the permeation according to the size of the diffusing moieties, and (ii) by side-chain modification, which enhances QA mobility and accordingly (selectively) increases the ion diffusion rate. We show that our methodology could successfully explain how the side-chain modification for PPO-QA membranes considerably increases the ion permeation while the methanol cross-over remains constant.

1 Introduction

Over the past few decades, we have witnessed tremendous growth in ion exchange membrane (IEM) applications in various industries, including water electrolysis,[1] the automotive industry,[2] redox flow batteries,[3] and polyelectrolyte membrane fuel cells.[4] Accordingly, fuel cell development has experienced considerable progress as a result of employing IEMs instead of traditional liquid electrolyte fuel cells.[2,4,5] IEMs, as the heart of these energy conversion devices, control the ion conduction and ensure the long-term performance of fuel cells.

Hydrophilic network management and the degree of phase separation between the hydrophilic and hydrophobic parts of the polymer are known to be the critical factors for water and ion transport through all types of IEMs.[6,7] The term "hydrophilic network management" refers to developing a water network at a standard water level to hinder membrane dehydration and maintain fuel cell efficiency. Preparing an optimal phase-separated network with desirable ion transport capabilities while maintaining the minimum hydration level has been a fresh challenge for scientists.[8–10] Thus, a clear correlation exists

[a]Department of Polymer and Color Engineering, Amirkabir University of Technology, 424 Hafez Ave., Tehran, Iran. E-mail: sharif@aut.ac.ir

[b]Department of Chemistry and Materials Innovation Factory, University of Liverpool, Liverpool L69 7ZD, UK. E-mail: hmakki@liverpool.ac.uk

† Electronic supplementary information (ESI) available. See https://doi.org/10.1039/d2ta04400e

This journal is © The Royal Society of Chemistry 2022

J. Mater. Chem. A, 2022, **10**, 18295–18307 | **18295**

between the morphology and ion transport properties of IEMs. In a previous study,[11] we investigated hydrophilic path formation and diffusivity of water/ions in a series of sulfonated polyether sulfone cation exchange membranes (CEMs). There, we established a quantitative relationship between the morphological parameters of the hydrophilic pathway in CEMs and their ion transport properties. We showed that the hydrophilic path, characterized by three measurable parameters, i.e., Pore Limiting Diameter (PLD), Largest Cavity Diameter (LCD), and Pore Size Distribution (PSD), plays a crucial role in controlling water and ion transport through the membranes. We established a quantitative relationship between these structural parameters and the diffusion coefficient of water and ions.

Using scarce and expensive platinum-based catalysts for CEMs hinders their widespread application in fuel cells.[12] Therefore, Anion Exchange Membranes (AEMs) modified with cationic groups are attractive alternatives that function well without platinum catalysts.[4,13] A variety of polymers, including poly(sulphone)s, poly(arylene ether)s, poly(styrene)s, poly(phenylene oxide)s, poly(ether ether ketone), and poly(olefin)s,[4,14–19] modified with a broad range of cationic groups[20–22] have been utilized for the production of AEMs. However, many AEMs show decreased performance over time and under different physical conditions. According to scientific reports,[9,23] this issue can be attributed to the inability of AEMs to manage and maintain a uniform hydrophilic pathway inside the membranes during their service life. Among them, polyphenylene oxide (PPO) based polymers functionalized by trimethylammonium quaternary groups and their derivatives showed high alkaline stability and great ion transport properties, making them a promising candidate in fuel cell applications.[24–27] Also, recent studies have shown that PPO backbones tethered with long flexible alkyl chains (more than four carbon units) as a spacer or extender bound to the cationic pendant group have better structural integrity and ion transport properties as compared to those without alkyl side-chains,[28–35] while the underlying mechanisms remained unclear.

Experimental and computational approaches have been used to explore the relationship between membrane morphology and ion transport behavior in functionalized PPO. For instance, Dang et al.[32] studied the effect of a flexible heptyl spacer on the hydroxide ion conductivity and hydrated membrane morphology of quaternary ammonium (QA) functionalized PPO (PPO-QA). Their SAXS results revealed that the heptyl spacer side-chain gives a more efficient phase separation between the ionomer and the backbone of the polymer as compared to conventional functionalized PPO without a spacer. They suggested that this could be attributed to the higher mobility of the QA group because of the flexible heptyl side-chain. In a related study,[30] they investigated the effect of cationic alkyl side-chains of different lengths and configurations tethered as a spacer, extender, and spacer + extender on hydroxide ion conductivity and morphology of PPO-QA membranes. They concluded that membranes with no spacer and extender show very poor phase separation and ionic clustering.

Moreover, phase separation is mitigated as an alkyl chain is tethered to the cationic group as an extender. In contrast, alkyl

spacer units (cationic head groups) facilitate ionic clustering as flexible alkyl fragments could provide appropriate local mobility for the cationic group to phase-separate from the polymer backbone. Along these lines, Lee[9] studied the effect of hydrophobic (alkyl) and hydrophilic (ethylene oxide) long spacers attached to the cationic groups on the phase-segregated behavior of PPO and polystyrene-ethylene-butylene-styrene (SEBS). The results showed that adding hydrophobic spacers improves nano-separation, and the membranes have better conductivity while having a decreased ion exchange capacity and water content. Also, they found that the stretched hydrophilic side-chains in the presence of water induce steric hindrance and prevent water and hydroxide ions from being transported through the polymer network. In very recent work, Molinero et al.[10,36] systematically explored the effect of alkyl spacer length (1–12 carbons) on ion diffusion in low water content (e.g., $\lambda = 5$) PPO-QA membranes. Their results showed that the alkyl side-chain length has a poor contribution to the width and clustering of the channels at a constant hydration level. At the same time, it enhances the anion diffusion coefficient. Their results suggest that the anion mobility increases while the width of the hydrophilic pathway remains constant.
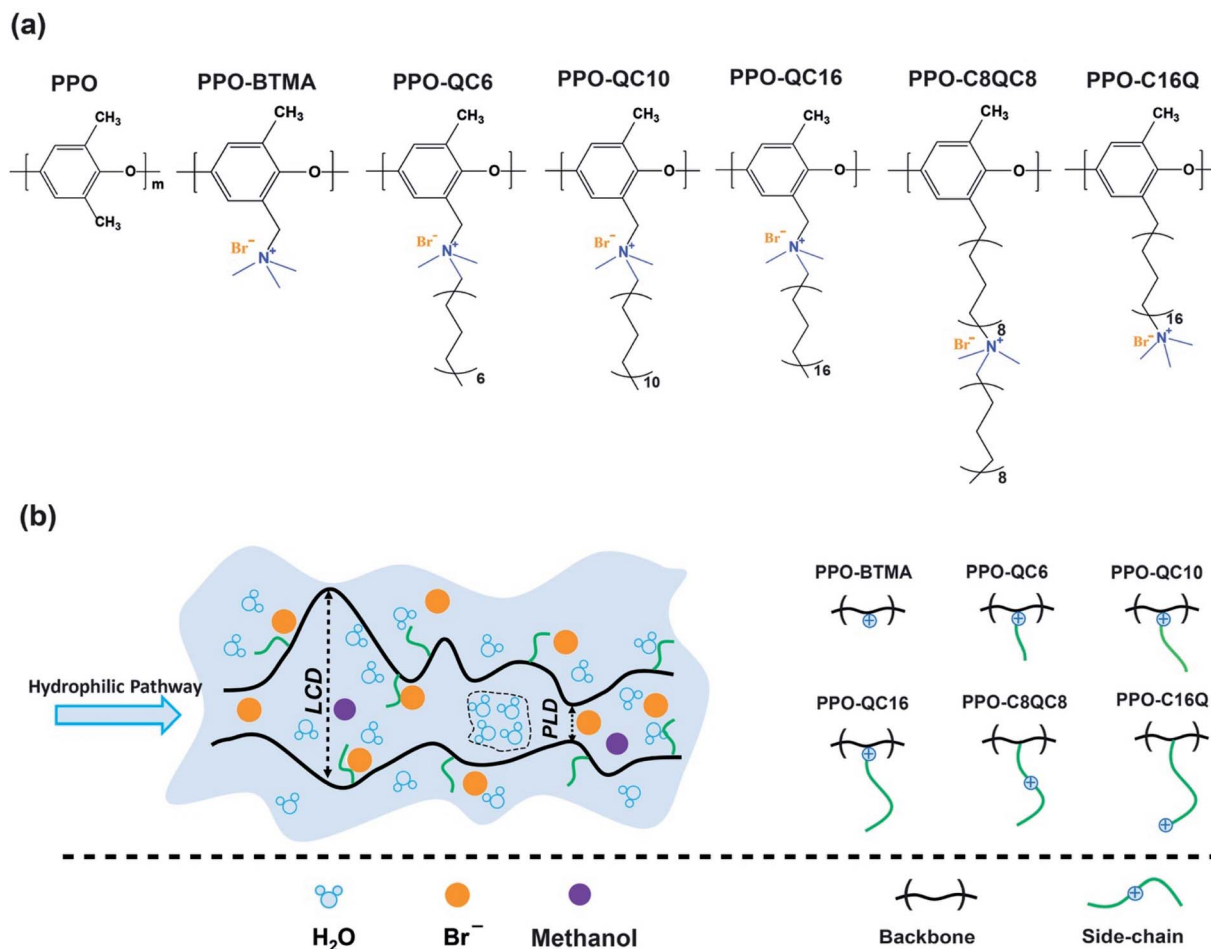
Despite multiple computational and experimental observations of the side-chain architecture effect on anion transport through AEMs, the impact of water content, side-chain length, and position of the cationic group on the morphology of the hydrophilic pathway and its relationship with ion transport behavior in modified AEMs with alkyl side-chains is still not fully understood, and a comprehensive examination is yet to be performed. In the current study, we performed atomistic-level molecular dynamics simulations for a series of cationic quaternary ammonium poly(2,6-dimethyl-1,4-phenylene oxide) (PPO-QA) membrane models with similar ionic content and different spacer and extender units. In the first part of this study, we aim to outline how water content and extender length ($n = 0, 6, 10,$ and 16) influence the morphology of the hydrophilic pathway and, accordingly, the water, anion (Br⁻) and methanol transport behavior. In the second part, we examine the effect of the cationic group position on a relatively long hydrophobic alkyl side-chain (16 carbon units) on the hydrophilic pathway morphology and water, anion and methanol diffusion coefficients at a constant hydration level. Also, we put forward a clear mechanism by which the position of QA on side-chains affects the anion transport. Our current study is focused on PPO-QA-based membranes; however, the resulting insight into the influence of structural parameters on transport properties and underlying mechanisms offers a rational molecular design strategy for new generations of polyelectrolyte membranes.

2 Methods

2.1 Molecular model approach

Model membranes consist of different types of cationic quaternary ammonium poly(2,6-dimethyl-1,4-phenylene oxide) (PPO-QA) random block-copolymers with a constant composition of 40% functionalized monomers and variable QA side-

18296 | J. Mater. Chem. A, 2022, 10, 18295–18307

This journal is © The Royal Society of Chemistry 2022

Scheme 1 (a) Chemical structure of functionalized and non-functionalized PPO monomers. (b) One-dimensional schematic illustration of the Pore Limiting Diameter (PLD) and Largest Cavity Diameter (LCD) parameters in a hydrated polymer structure.

chain configurations in the presence of Br$^-$ ions. Monomers are functionalized by quaternary ammonium with and without an alkyl side-chain (0, 6, 10, and 16 carbon units) as extender, spacer, and spacer + extender attached to the cationic groups. Each polymer chain is constructed by 20 monomers, 8 of which are randomly functionalized by cationic quaternary ammonium. The chemical structure of different forms of functionalized and non-functionalized monomers of the PPO-QA chain is depicted in Scheme 1a. We named the membranes based on side-chain structure and position of cationic groups. For instance, PPO-BTMA stands for a polymer with cationic groups attached to the polymer backbone without an alkyl side-chain ($n = 0$), and PPO-C8QC8 refers to a polymer with a cationic group placed in the middle of the 16-carbon length alkyl side-chain.

It is worth noting that our MD simulations utilize short polymer chains exhibiting enhanced end-group effects as compared to experimental systems with longer chains. However, all-atom MD simulations of polymer solutions with long chains are problematic since the chain structures do not equilibrate within the achievable duration of such simulations, which corresponds to a few hundreds of ns. Since we are not interested in the diffusive dynamics of the chains but rather in the diffusive dynamics of water and anions, and since the

polymer solution structure does not depend much on chain length in the so-called semi-dilute solution regime,[37] the chain length chosen by us should allow us to draw meaningful conclusions from our simulations. Also, an in-depth literature review of the recent works on similar systems shows that equal or even shorter polymer chain lengths are typically used in MD simulations.[25,38–40] Simulations of hydrated membranes have been performed at different (intermediate) hydration levels in AEMs ranging from $\lambda = 2$ to 15, where λ is the number of water molecules per fixed ionic (quaternary ammonium) group. λ can be converted to water content (wt%) using eqn (1).

$$\text{wt\% } H_2O = \frac{\lambda \times \text{IEC} \times M_{\text{water}}}{10} \tag{1}$$

where wt% H_2O is the weight percent of water, IEC is ion exchange capacity in mequiv g^{-1} and M_{water} is the molecular weight of water in g mol^{-1}. $\lambda = 0$ is also used to calculate the density of dried membranes.

2.2 Simulation details

Gromacs (version 2020-2)[41] was employed for all MD simulations of AEMs using a leap-frog integration algorithm. We

applied the OPLS-AA potential energy function,[42] which has previously been effectively applied to polyelectrolytes,[40,43–45] to define intermolecular bonded and non-bonded interaction parameters of AEMs. The individual partial charges of atoms in polyelectrolyte chains were assigned from DFT calculations using Gaussian 16 with the B3LYP method and 6-31++g(d,p) basis set, respectively.[46,47] Partial charges of PPO-BTMA, as an example, are shown in Fig. S1 and Table S1 in the ESI.† The Particle Mesh Ewald (PME) method was employed in all runs to describe the long-range force of electrostatic interactions among partial charges with a cut-off distance of 1 nm. The van der Waals particle pair interactions are also described by the 12–6 Lennard-Jones potential, with the cut-off distance set at 0.9 nm. In addition, a TIP3P water model[48] was selected owing to its fine reproduction of the diffusion coefficient. To accurately recover the density of the system, long-range dispersion and pressure corrections were applied. The LINCS algorithm was implemented to restrain covalent bonds of hydrogen atoms.[49] Temperature and pressure are controlled using the V-rescale thermostat at 295 K and the Parrinello–Rahman barostat at 1 bar with a relaxation time of 0.1 ps and 2 ps, respectively. Finally, a time step of 2 fs was applied for the overall production run. The VMD software was used to create all simulation visualizations.[50]

After the selection of appropriate methods and ensembles, the next critical stage is choosing the system size to avoid finite-size effects and inaccuracies of calculation. For this purpose, identical simulations were carried out for different box sizes with a varied number of polyelectrolyte chains, *e.g.*, 20, 30, 40, 50, and 60 chains, and several structural and physical parameters were examined (see Fig. S2 in the ESI†). Analysis showed no specific discrepancy for the simulation boxes above 20 chains, so the system with 40 polymer chains was selected as an optimal system size to have a large enough system. The procedure of relaxation and simulation of the membranes is provided in the following section.

To construct the simulation box, 40 polyelectrolyte chains were added to a large enough cubic box with periodic boundary conditions in three dimensions to eliminate edge effects.[51] Following that, 320 Br⁻ ions and an appropriate number of water molecules depending on the defined hydration levels (λ) were dispersed randomly into the simulation box, so the system was totally uncharged. All system compositions are reported in Table S2 of the ESI.† The equilibration process is discussed in detail in the ESI† (Section 3). Equilibrated cell sizes were ~6.2–8.2 nm with roughly 24 000 to 47 000 atoms for different hydrated membranes. It should be noted that separate simulations, with 320 additional methanol molecules in each simulation box (for all AEMs), have been performed to assess methanol diffusion in comparison with water/ion diffusion. Each simulation was repeated three times, and an average of the results was reported with standard errors. Also, the last 5 ns of all production runs are ignored for all analyses.

Using the decay behavior of the time autocorrelation function of the squared radius of gyration, we characterized the relaxation properties of different polymer chains. The results are provided in the ESI in Fig. S3.† As shown in Fig. S3,† the squared radius of the gyration autocorrelation function dropped to zero in the early times of simulation, and all the samples show a relaxation time of less than 13 ns. These results indicate that the relaxation process was efficient. The 100 ns simulation time is long enough for the equilibration of the system and provides independent configurations for averaging the desired properties. All the samples followed a similar pattern at other hydration levels.

2.3 Analyses

2.3.1 Static characterization. The radial distribution function $g_{A-B}(r)$ and coordination number (CN) were utilized to characterize the structural properties and interactions of cation–cation, cation–water, water–water, and cation–anion in hydrated AEMs. The radial distribution function is expressed as the probability of local distribution of particle A around particle B as a function of distance. Coordination number (CN) provides the total number of neighbors of a central particle of interest within a preset distance of r. In addition, water cluster analysis was applied to investigate the propensity of water molecules to form a nanoscale hydrophilic channel structure. A water cluster is defined as a hydrogen-bonded network of water molecules in which the oxygen atom of a water molecule is synergized together at a specified cut-off distance. In this study, this distance is fixed at 0.37 nm, as determined by the first minimum of $g_{Ow-Ow}(r)$ of the bulk state TIP3P water model at 295 K.

A computational tool, Poreblazer (V4.0),[52] has been used to characterize the porous membrane structure. Poreblazer provides several quantitative parameters of the porous polyelectrolyte matrix, including Largest Cavity Diameter (LCD), Pore Limiting Diameter (PLD), and Pore Size Distribution (PSD) that can be utilized for hydrophilic channel characterization. PLD and LCD are schematically depicted in Scheme 1b. For this purpose, first, we selected several frames of dried membrane for every 1 ns from 70 to 95 ns and reported an average of the calculated structural parameters with standard deviation.

2.3.2 Dynamic characterization. The diffusion of small species, *e.g.*, water and ions in polyelectrolyte membranes, is a complex, multifaceted atomistic-level phenomenon. To determine the mobility of water and anions, we evaluated the self-diffusion coefficient from the linear part of the mean squared displacement plot using Einstein's relation in n-dimensional Brownian motion (eqn (2)).

$$\langle (r_j(t) - r_j(0))^2 \rangle = \mathrm{MSD}(t) = 2dDt \tag{2}$$

where MSD is the mean-squared displacement, D is the diffusion coefficient, and d is the topological dimension equal to 3 (in our study) for three-dimensional motion.[53] This equation refers to isotropic uniform normal diffusion, where the continuous random walk (CTRW) is a Brownian Motion (BM). However, the anomalous diffusion behavior emerges in a highly heterogeneous configuration where the diffusion behavior of diffusing species deviates from a continuous regular random walk. This is the case in polymer and porous networks. According to our case study, in polyelectrolyte structures, water

and ion species always show anomalous transport behavior, especially at very low temperatures and hydration levels, due to steric hindrance exerted by the polymer structure and direct interaction of water and ions with functional groups.[54] In anomalous diffusion, MSD is non-linear with time. In this regard, for a deeper understanding of the nature of diffusion and to distinguish different forms of diffusion mechanisms, a generic version of Einstein's equation can be expressed with the anomalous diffusion exponent (n) as

$$\langle (r_j(t) - r_j(0))^2 \rangle = \text{MSD} \sim 2dD_a t^n \tag{3}$$

with $n = 1$ giving normal or Fickian diffusion, $n > 1$ indicating super-diffusion behavior (faster diffusion than normal diffusion) and $0 < n < 1$ showing sub-diffusion (slower diffusion than normal diffusion).[44,55] Also, D_a is the anomalous diffusion coefficient (in the anomalous diffusion regime). Here, despite the normal diffusion behavior of some cases in specific time periods, we consider all diffusion coefficients obtained from simulation as anomalous diffusion coefficients. In porous structures, e.g., polymer structures, some particles of diffusive species (here water and ions) get stuck in holes for an extended period, giving slow diffusion termed a sub-diffusive process. To offer a clear picture of the hydration effect on diffusion behavior, the anomalous diffusion exponent behavior was plotted as a function of time to demonstrate the degree of deviation from the normal diffusion mechanism during the simulation. The anomalous diffusion exponent is obtained using eqn (4).

$$n(t) = \frac{d \ln \langle \Delta r^2(t) \rangle}{d \ln t}. \tag{4}$$

3   Results and discussion

3.1   Validation of the simulations

To validate the selected force field and model membranes, we evaluated the dry mass density and water diffusion coefficient of hydrated membranes by reference experimental data.[56] For instance, the dry mass density of PPO-BTMA obtained from the simulation was 1.25 g cm^{-3}, which is in good agreement, i.e., less than 5% difference, with the experimentally reported value equal to 1.19 g cm^{-3}. Also, the theoretical diffusion coefficients of water showed a similar trend in the range of the defined hydration levels. Density and diffusion data of experiments and simulations are provided in ESI Tables S3 and S4.† Therefore, the simulations are validated for further analysis based on the density and simulated diffusion results.

3.2   Effect of the side-chain extender and hydration level

3.2.1   Radial distribution function and coordination number of the ionomer, water, and anion. Polyelectrolyte membranes can modulate their structural architecture as a function of hydration level. On the other hand, the distribution of quaternary ammonium groups is an essential factor controlling nano-phase segregation and water channel formation in the PPO-QA. This issue is explored by using the pair
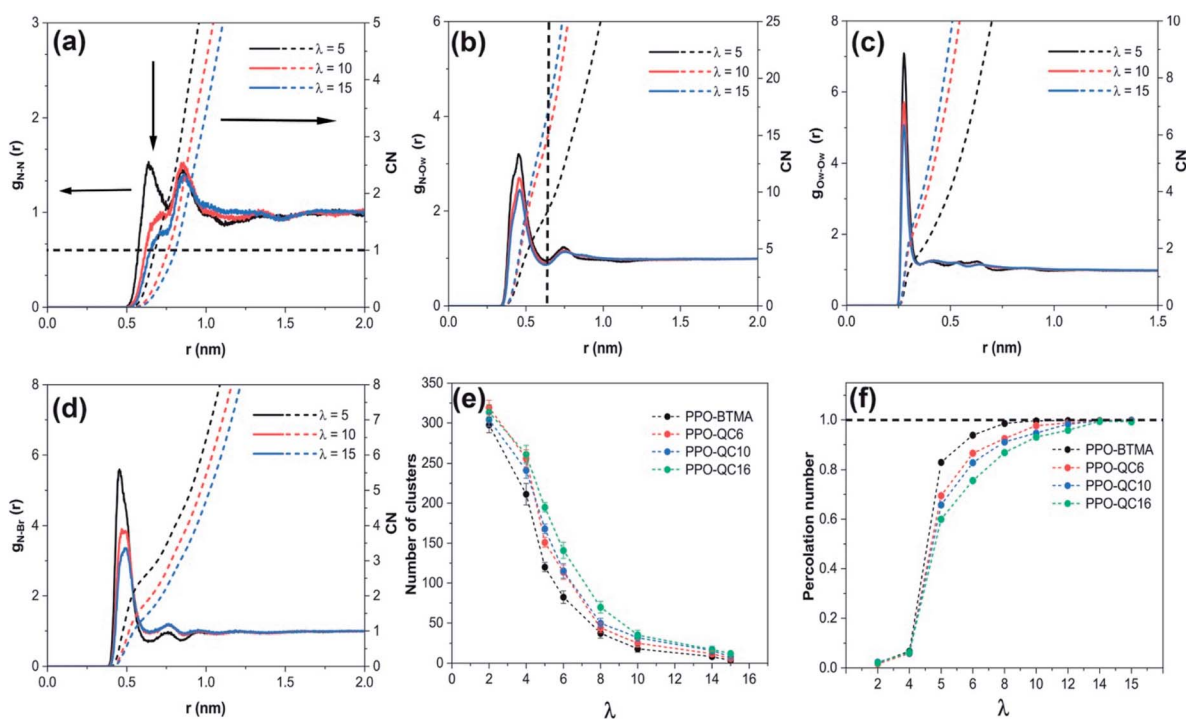

Fig. 1   The radial distribution function of (a) nitrogen–nitrogen, $g_{N-N}(r)$, (b) nitrogen–oxygen (water), $g_{N-Ow}(r)$, (c) oxygen (water)–oxygen (water), $g_{Ow-Ow}(r)$, and (d) nitrogen–Br$^-$, $g_{N-Br}(r)$, for the PPO-BTMA membrane, (e) number of clusters as a function of hydration level and (f) normalized cluster size as a function of hydration level.

distribution function ($g_{N-N}(r)$) and coordination number (CN) of QA at different hydration levels for membranes with different alkyl extender lengths ($n = 0, 6, 10, 16$). Fig. 1a illustrates the $g_{N-N}(r)$ and CN of PPO-BTMA at different hydration levels. It has been clearly shown that the $g_{N-N}(r)$ has two distinct peaks at $\lambda = 5$: the first peak at ≈ 0.64 nm and the second at ≈ 0.85, which decrease in height, shift toward more distant positions and merge into a single weaker peak at $\lambda = 15$. Due to the hydrophilic nature of QA, water molecules tend to solvate it. Therefore, by increasing the number of water molecules per N^+ (increase in λ), more water molecules are available to push cationic groups towards more distant positions. The correlation between N^+ cationic groups is similar for all membranes as hydration increases, while the second peak is more pronounced for PPO-QC16 indicating more distant cationic groups due to the greater steric hindrance exerted by the long alkyl extender around QA that maintains N–N pairs farther apart (see Fig. S4 in the ESI†). Also, the CN plot shows that in PPO-BTMA, at least one neighboring N^+ group exists at a distance of ≈ 0.67 nm at $\lambda = 5$. However, this distance increased to ≈ 0.81 nm at $\lambda = 15$. The same trend was also found for the others, with the distance between the neighboring groups for PPO-QC16 increasing from ≈ 0.75 nm to ≈ 0.85 nm at $\lambda = 5$ and $\lambda = 15$, respectively (Fig. S4 in the ESI†).

We investigated the radial distribution function of the N–Ow (water molecules), $g_{N-Ow}(r)$, and CN to study the structure of water channels and solvation of the N^+ cationic groups in water (Fig. 1b). For all hydration levels, $g_{N-Ow}(r)$ for PPO-BTMA exhibits pronounced peaks commonly at ≈ 0.45 nm and ≈ 0.74 nm, which correspond to the first and second hydration shells surrounding the cationic group. Furthermore, when hydration increases, the peak height decreases owing to the solvation effect, as more water molecules seek to wet cationic groups. In addition, based on CN, the average number of water molecules around cationic groups increases from ≈ 8.5 to ≈ 18 as hydration increases from $\lambda = 5$ to $\lambda = 15$. A similar trend but with elevated peaks was observed for the other membrane with the increase in side-chain length, especially for PPO-QC16. The higher peaks at the same hydration levels are attributed to the stronger interaction between water molecules and QA. Steric hindrance exerted by the long side-chain extender holds water molecules near cationic groups for a more significant period and, on the other hand, fewer water molecules stand for longer times near cationic groups because of hydrophobic side-chain hindrance (Fig. S4 in the ESI†).

By using the radial distribution function of oxygen (water)–oxygen (water) ($g_{Ow-Ow}(r)$) and CN, we investigated the internal structure of water molecules at different hydration levels to study the water molecule's mutual tendency (Fig. 1c). As is evident, first, a distinct peak is observed at ≈ 0.27 nm for the PPO-BTMA membrane, which is ascribed to the first hydration shell of the water molecule around each water molecule. Second, CN increases with an increase in water content due to the solvation effect and overall packing of water molecules. Other membranes exhibited the same behavior but with a sharper peak height for membranes with longer side-chains (e.g., PPO-QC16) at constant hydration. This is attributed to

more separated water molecules in the membrane network which shows that each water molecule holds fewer water molecules around itself (Fig. S4 of the ESI†).

Anion transport is another essential aspect controlling membrane efficiency. To further look into this, we analyzed $g_{N-Br}(r)$ and CN to study the correlation between cationic quaternary ammonium and Br^- ions. As shown in Fig. 1d, at $\lambda = 5$ for the PPO-BTMA membrane, the first strong and second weak peaks emerged at ≈ 0.45 nm and ≈ 0.75 nm, respectively. An increase in hydration decreases peak height. It shifts it to a more distant position from ≈ 0.45 nm at $\lambda = 5$ to ≈ 0.50 nm at $\lambda = 15$, indicating that additional water molecules weaken electrostatic interactions between the cationic group and anions and move them to farther distances. This trend is comparable to that in other membranes; however, the first peak heights are stronger than those of other membranes in PPO-QC16 (see Fig. S4 in the ESI†), indicating that cationic groups and Br^- ions have stronger electrostatic interaction again due to the presence of the alkyl side-chain extender that holds and hinders anions from moving from one cationic group to another.

3.2.2 Water cluster and hydrophilic pathway.

It has been proven that the formation of an optimum hydrophilic structure can improve ionic mobility and conductivity.[57] Water molecules are inclined to form clusters with the increase in hydration level, which is a determining factor in constructing a uniform hydrogen-bonded water network for water and ion transport.

We analyzed the number of clusters and cluster percolation thresholds to learn more about the hydrophilic channel nanostructure. Fig. 1e shows the number of clusters as a function of water content in different membranes. As shown, at e.g. $\lambda = 5$, small clusters of water molecules are entirely isolated. With the increase in hydration level in all membranes, water clusters grow and draw closer to each other, forming larger branches at high hydration levels. Accordingly, the number of clusters decreases. The PPO-BTMA membrane shows a smaller number of clusters at the same hydration level than other membranes. As discussed in Fig. 1c, fewer water molecules cover each other in the membrane with the largest side-chain extender resulting in smaller cluster size. Hence, to gain more insight into the formation of percolated water channels and the effect of quaternary ammonium position, we analyzed the normalized cluster size to study the percolation threshold of the water cluster:

$$\text{Normalized cluster size} = \frac{\text{largest cluster size}}{\text{whole number of water molecules in the box}} \quad (5)$$

Here, the normalized cluster size is used to estimate the function of water molecules that form the largest hydrogen-bonded water network. A similar trend to the number of clusters is observed for other membranes. As shown in Fig. 1f, about 2% of water molecules in hydrated membranes belong to the largest cluster at very low hydration levels. All the membranes show substantial growth in cluster size at increasing hydration levels such that, at $\lambda = 5$, nearly 83% of water molecules belong

18300 | J. Mater. Chem. A, 2022, 10, 18295–18307

This journal is © The Royal Society of Chemistry 2022

to a single cluster in the PPO-BTMA membrane. In comparison, this number is less than 70% for the others. This trend continues up to $\lambda = 10$, where an almost complete hydrogen-bonded water cluster forms in PPO-BTMA and other membranes reach close to the percolation line at higher hydration levels. This means that forming a percolated water network depends on the water content and side-chain extender length.

To better visualize the water network morphology, typical simulation box snapshots of hydrated PPO-BTMA at different hydration levels are shown in Fig. 2a. These snapshots provide a nanoscale picture of water clustering inside the membrane, similar to the pictures that can be provided by cryogenic transmission electron microscopy (cryo-TEM)[58] and X-ray computed tomography (CT)[59] tools for hydrated membranes. It can be observed that small isolated clusters are distributed into the polymer matrix at the lowest water concentration, $\lambda = 5$. As the hydration increases up to $\lambda = 15$, small clusters grow, and the hydrophilic network is more interconnected, providing a fully developed hydrophilic domain for water and ion transport.

In what follows, we examine several geometrical factors contributing to water and anion diffusion, *e.g.*, PLD, LCD, and PSD, as discussed in our recent work[11] to further understand the water channel evolution in the polymer matrix function of water content and polymer architecture.

As previously stated, water molecules move from one pore to the next while passing through bottlenecks. The bottleneck size highly depends on water content and thermal fluctuations of polymer chains.[60] PLD, the water channel bottleneck, is a critical diameter for water and ion diffusion. If PLD is larger than the water or Br^- ion diameter, water and ions can pass from one pore to the next in cationic exchange membranes.[11] Here, to trace the geometry of pores for water and anion diffusion, we defined PLD based on the selected water model and Br^- ion diameter, *i.e.*, ≈ 0.31 nm and ≈ 0.39 nm, respectively. As shown in Fig. 2b, the PLD of all membranes is far less than the critical diameter both for water and anions before $\lambda = 8$. But, PLD increases as hydration increases such that all membranes, except PPO-QC16, cross the PLD line of the water molecule at $\lambda = 10$, even though they are still smaller than the ion size. This means that Br^- ions cannot freely move through all pores in the membrane.

Finally, all membranes pass the PLD line of the ion at $\lambda = 15$. Results for water are perfectly consistent with the number of clusters and normalized cluster size analyses, indicating that when PLD goes over the critical line, a noticeable shift in water channel structure occurs.

LCD is another critical parameter determining the maximum pore size in a heterogeneous polymer network. As shown in Fig. 2c, LCD increases in all membranes as water content rises so that all membranes have the largest LCD at $\lambda =$
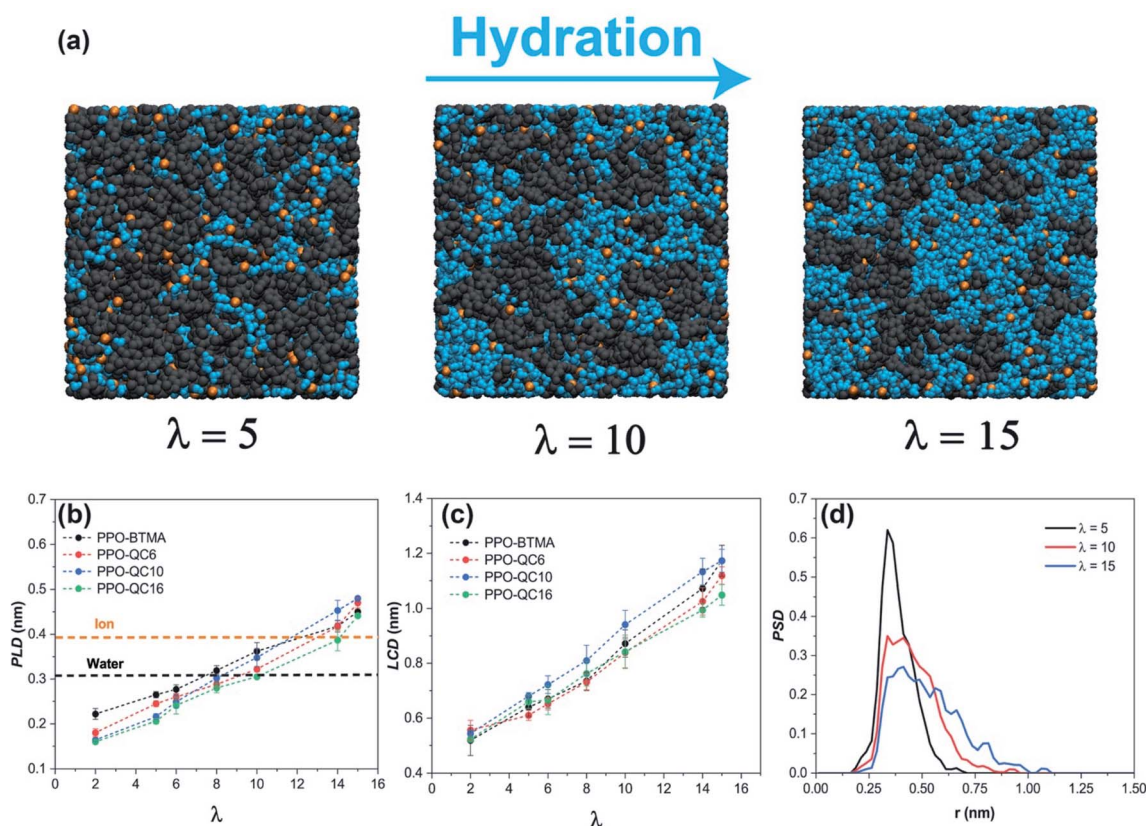

Fig. 2 (a) Cross-section snapshots of hydrated PPO-BTMA membranes at $\lambda = 5$, 10, and 15. The polymer chain is dark gray, Br^- is indicated in orange, and the cyan surface represents water regions. (b) Pore limiting diameter (PLD) as a function of hydration levels. (c) Largest cavity diameter (LCD) as a function of hydration levels. (d) Pore size distribution (PSD) for PPO-BTMA at different hydration levels.

15. This is attributed to the more extended polymer network because of higher water content. The similar trend of PLD and LCD as a function of hydration shows that the membrane's pore and bottleneck diameters grow with a more or less identical underlying process.

PSD is the final structural feature we wish to discuss to give a complete picture of the hydrophilic channel width distribution occupied by water and anions in a disordered polymer structure. Porous network transport properties are governed by the PSD and how pores are topologically structured, completing our diffusion picture in polymer membranes. The PSD variation of the PPO-BTMA membrane at different hydration levels is presented in Fig. 2d. A single narrow peak associated with the largest pore size exists in the heterogeneous structure, *i.e.*, at 0.33 nm for $\lambda = 5$, which broadens in distribution and moves to farther distances with increasing water content, reflecting the presence of larger pores with different distribution forms in the structure. Similar trends are observed for other membranes (Fig. S5 in the ESI†). Increased hydration broadens the PSD and improves pore connectivity. It should be noted that in real applications, the chemistry and architecture of the polymer determine the amount of water taken up.[61] Thus, the hydration level cannot be selectively adjusted under real conditions as is done in simulations. However, our selected range of hydration levels spans a typical range of hydration levels for this class of membranes.[25,29,56,62] Thus, the morphological parameters of the hydrophilic pathway of membranes at their actual (and experimentally obtained) hydration level are accessible in the data shown in Fig. 2b–d.

3.2.3 Dynamic characterization. The primary role of the present study is to explore the diffusion behavior of water and ions as a tool to guide the design of AEMs with a tailored structure. The main mechanisms of diffusion have been studied in Section 2 in detail. It has been proved that the diffusion
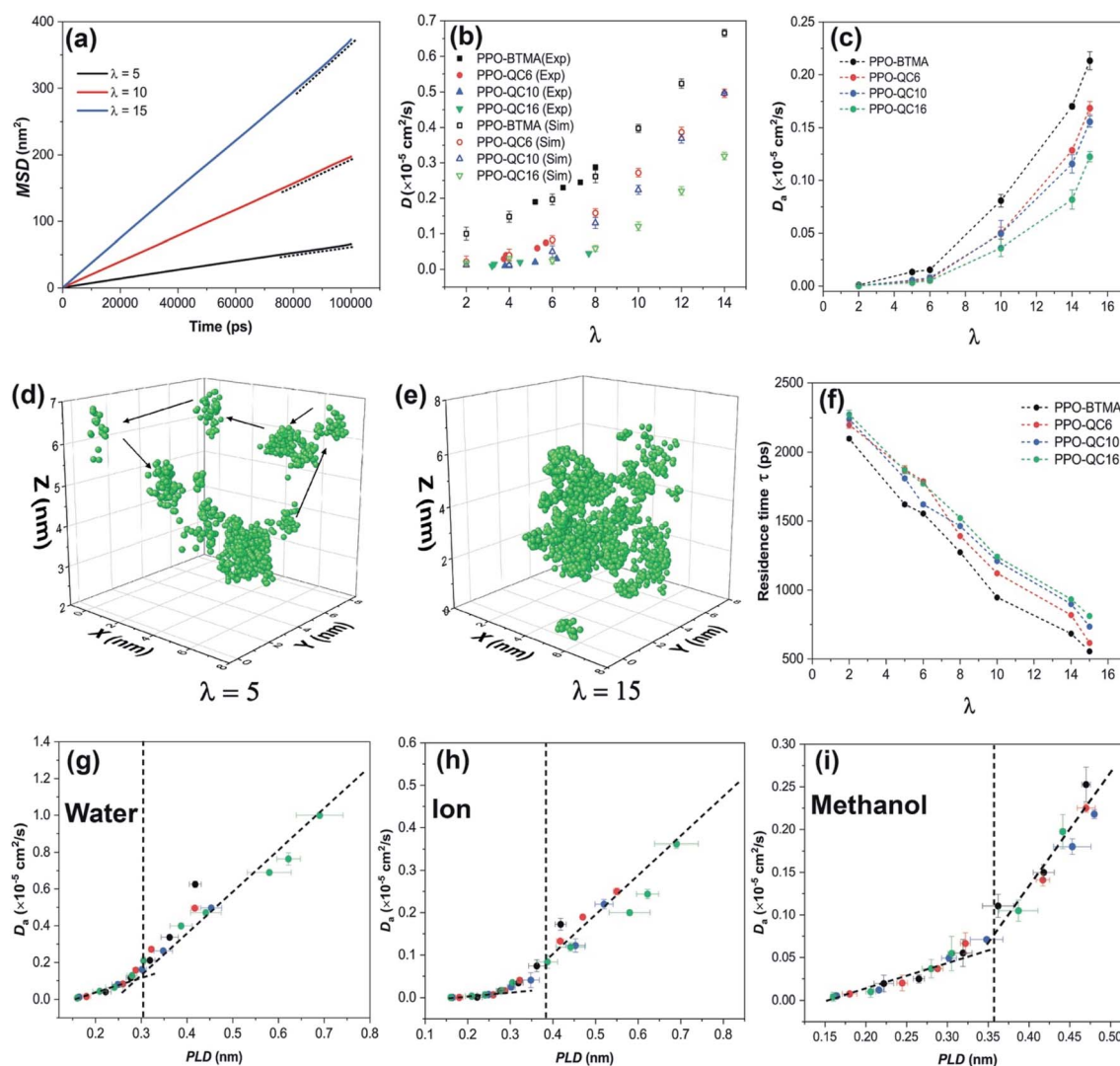

Fig. 3 (a) MSD of water in PPO-QC16 at different hydration levels, (b) experimental diffusion coefficient[56] and anomalous diffusion coefficient of water in hydrated membranes obtained from simulation, (c) anomalous diffusion coefficient of anions in hydrated membranes, (d and e) the trajectory of a single water molecule, respectively, at $\lambda = 5$ and $\lambda = 15$, (f) residence time of water near cationic groups at various hydration levels, and (g) anomalous diffusion coefficients of water, (h) the Br$^-$ ion and (i) methanol as a function of PLD.

18302 | *J. Mater. Chem. A*, 2022, **10**, 18295–18307

This journal is © The Royal Society of Chemistry 2022

coefficient in polymers follows a concentration-dependent behavior.[44,63] Therefore, in the current section, we investigate the effect of water content on transport behavior in PPO-QA membranes with different side-chain sizes. Fig. 3a presents the MSD of PPO-BTMA at different hydration levels. It turns out that MSD curves follow a linear pattern, with the slope increasing significantly as the hydration level rises. This curve gives information about the high dynamics of the water molecule as a function of water content. MSD of PPO-BTMA shows a steeper slope than PPO-QC16 (Fig. S6†) at the same λ. This is attributed to the well-developed hydrophilic channel structure in the PPO-BTMA membrane compared to PPO-QC16 justifying fewer barriers and higher mobility of water molecules as also hypothesized in experimental studies.[56] The anomalous diffusion coefficient D_a of water is determined from the linear regime of the MSD curve[64] and shown in Fig. 3b. As shown, D_a of water increases at elevated hydration levels. Also, D_a of Br^- ions is presented in Fig. 3c. The same trend is observed for D_a of ions; however, D_a of ions is, on average, five times smaller than that of water molecules at the same hydration levels, which is attributed to the different sizes and electrostatic interactions of water and anions with the ionomers.[65] The diffusion coefficient of methanol is also available in ESI Fig. S7.†

It has been proven that both water and ions show anomalous subdiffusion behavior in the polymer matrix.[65,66] To gain a better insight into the transport behavior of water in PPO-QA membranes, we determined the anomalous diffusion exponent of water as a function of water content. Fig. S8a in the ESI† presents the anomalous diffusion exponent of water in the PPO-BTMA membrane at different hydration levels. As shown, anomalous diffusion exponents increase as time elapses. However, at $\lambda = 5$, the diffusion of water molecules in the membrane reveals anomalous subdiffusion characteristics with no apparent indicators of approaching the normal diffusion ($n = 1$). This behavior is attributed to the high tortuosity and isolated water clusters in polymer membranes preventing water molecules from being freely transported in water channels. At increasing hydration levels, the anomalous diffusion exponent comes closer to unity, where the water molecules may reach a diffusive limit (Fickian diffusion). However, the PPO-QC16 membrane follows a poor scenario, as shown in Fig. S8 of the ESI,† indicating that an anomalous diffusion exponent is more distant from the unity line even at long simulation times. It can be concluded that, as hydration increases and a well-developed water network forms, the transport behavior is less sensitive to the interaction of water and charged groups mediating normal diffusion. Another critical parameter is polymer proportion and chemical structure. Water diffusion in neutral polymers revealed that the strength of water molecule trapping in the polymer matrix could delay normal diffusion behavior to more extended periods, which are not usually accessible in MD simulations.[67,68]

To understand the origin of the non-Fickian behavior, a 10 ns single water trajectory at $\lambda = 5$ and $\lambda = 15$ in PPO-BTMA is shown in Fig. 3d and e. It can be seen that, at $\lambda = 5$, the trajectory of water molecules is more restricted at specific locations for a while and they jump to the next site, which is consistent with the reported jump-diffusion mechanism of water at low hydration levels.[69] We hypothesize that these locations are isolated water clusters in which water molecules hop from one to the next due to temperature fluctuations. At $\lambda = 15$, on the other hand, the water molecules are more randomly distributed, and continuum mobility makes a significant contribution. Water molecules and ions have more freedom to traverse continuously along the polymer matrix.

To evaluate the influence of side-chain length on anomalous diffusion behavior, we measured the local residence time of water molecules near QA. Residence time relates to how long (on average) water molecules reside in the preset radial cut-off region around cationic groups. Using the radial distribution function, we set this cut-off to ≈ 0.61 nm, which corresponds to the first hydration shell radius around QA groups and is estimated by the first minimum of $g_{N-Ow}(r)$. The method of determining residence time is described in the ESI† (Section 10). According to Fig. 3f, all the membranes follow a decreasing trend as the hydration level increases. For instance, water molecules spend on average 1620 ps in the first hydration shell of the cationic groups in PPO-BTMA, while this time is 1866 ps for PPO-QC16 at $\lambda = 5$. This time decreases to 555 ps for PPO-BTMA and 812 ps for the PPO-QC16 membrane at $\lambda = 15$. Also, other membranes follow a moderate behavior.

Last, we summarize the discussion in this section by correlating water, ion, and methanol diffusion with PLD. PLD-D_a data for all the membranes that have been studied so far are shown in Fig. 3g (D_a of water molecules), Fig. 3h (D_a of Br^- ions), and Fig. 3i (D_a of methanol molecules). The trends of both water and ion-related graphs are in full agreement with the hypothesis put forward for CEMs in a previous work:[11] the critical role of PLD in controlling the diffusion coefficient of water and anions. This agreement shows that the morphology of the hydrophilic pathway plays a crucial role in maintaining ion transport for both CEMs and AEMs in a similar way.

As noted by other studies,[70] methanol cross-over in AEMs has a detrimental effect on fuel cell performance; hence, one of the key roles of ion exchange membranes is to hinder the methanol cross-over. Thus, we studied methanol diffusion in similar systems but containing additional methanol molecules. As shown in Fig. 3i, a similar behavior was observed for the PLD-D_a plot of methanol showing increased methanol diffusion coefficients as PLD crosses the critical value (an approximate methanol diameter is 0.36 nm (ref. 71)). According to this finding, methanol cross-over through the membrane increases as the hydrophilic channel width increases, in a manner that is comparable to that of water and ions.

We showed that increasing the hydration level significantly enhances the ion transport properties due to the formation of a more uniform and interconnected hydrophilic pathway. We also successfully examined the quantitative parameters in describing hydrophilic pathway morphology and correlated them to the water/ion diffusion coefficient for PPO-QA membranes. Moreover, we showed that alkyl side-chain extenders hinder water/ion transport through membranes, as evidenced by experiments.[56] However, we proved that this is due to the morphological changes in the hydrophilic pathway so

This journal is © The Royal Society of Chemistry 2022

J. Mater. Chem. A, 2022, **10**, 18295–18307 | **18303**

that alkyl side-chain extenders isolate QA groups from the water network, which results in isolated water clusters. On the other hand, when PLD rises, the methanol diffusion coefficient rises as well, which may restrict the performance of the membrane at very high hydration levels.

3.3 Effect of QA position on the alkyl side-chain

In this part, we aim to discuss the effect of the QA position, *i.e.*, near the backbone, in the middle, and at the end of the alkyl side-chain, on the morphological and anion transport properties of the membranes. Note that PPO-QC16 represents a polymer with QA attached to the polymer backbone, PPO-C8QC8 represents a polymer with QA placed in the middle, and PPO-C16Q represents a polymer with QA at the end of the alkyl side-chain.

First, we analyzed $g_{N-N}(r)$ and $g_{N-Ow}(r)$ to investigate the hydrophilic channel structure of various membranes. As shown in Fig. 4a and b, PPO-QC16 and PPO-C8QC8 show similar $g_{N-N}(r)$ and $g_{N-Ow}(r)$, while N^+ in PPO-C16Q shows a much stronger interaction with other QA and water molecules. The position of N^+ at the end of the alkyl side-chain results in pulling this group towards the water phase and placing more N^+ groups at the polymer–water interface, as also discovered by SAXS analysis previously for similar membranes.[30,32] Furthermore, the average number of water molecules around QA, the CN in PPO-QC16 and PPO-C8QC8 membranes (Fig. 4b), is less than λ (*e.g.*, CN $\approx$ 13 at $\lambda = 15$), suggesting that some QA groups are located inside the polymer phase. However, in PPO-C16Q membranes,

CN $\approx$ 16.8 and larger than $\lambda = 15$, implying that more QA is placed at the interface of the polymer and water. However, the typical simulation box snapshots shown in Fig. 4c suggest that the QA position has a negligible impact on the nano-phase separation between the polymer and water in the membranes.

We further analyzed the number of clusters of different membranes at $\lambda = 15$. As shown in Fig. 5a, the decrease in the number of clusters is also negligible as cationic groups move to the end of the alkyl side-chain. To quantify the hydrophilic pathway characteristics, we also looked at the PLD, LCD, and PSD of different membranes (Fig. 5b and c). As shown, they remain approximately constant with changing the position of the QA on the alkyl side-chain as well, which is in agreement with the qualitative perception of the hydrophilic membranes from Fig. 4c. We also analyzed the polymeric phase of the membrane by removing all polymer molecules and anions from the simulation box and calculating the PSD, this time for the polymeric phase. As depicted in Fig. 5d, the polymer region size distribution also shows no considerable change as the position of the QA is changed.

Therefore, these results confirm that the morphology of the membrane is more or less insensitive to the position of QA in a fixed side-chain length.

As shown in Fig. 5b, the hydrophilic channel width of the three membranes at $\lambda = 15$ is larger than that of all three diffusing species based on their previously mentioned sizes (*i.e.*, water = 0.31 nm, Br^- ion = 0.39 nm, and methanol = 0.36 nm). At the same time, the channel width is kept more or less
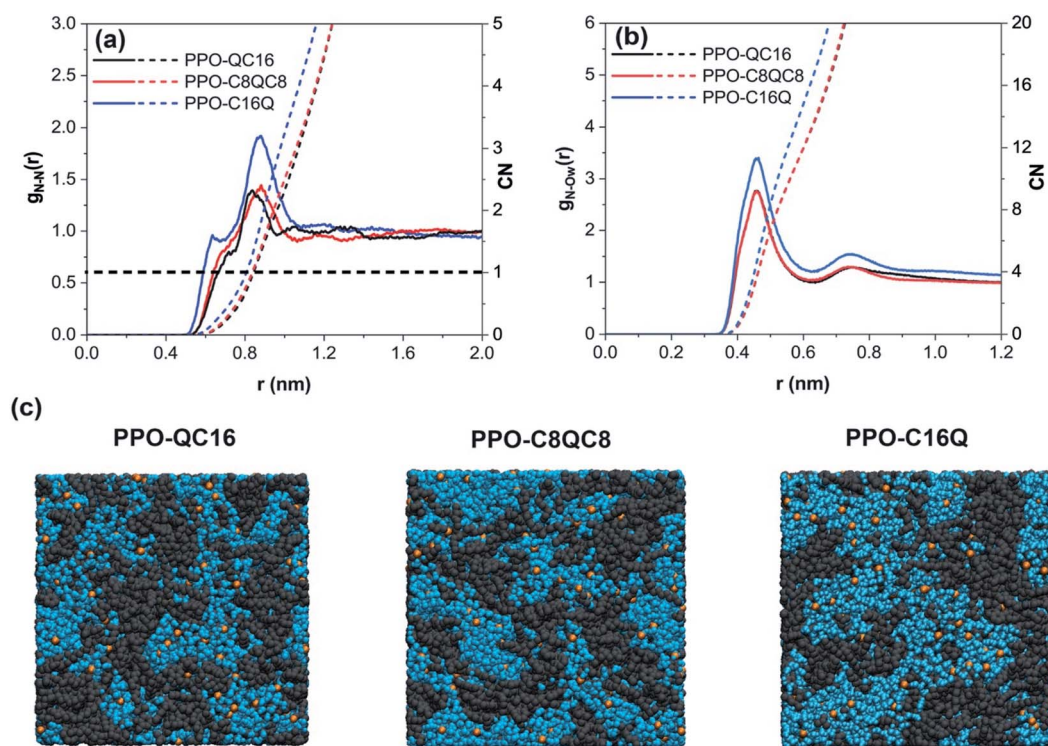

Fig. 4 (a) $g_{N-N}(r)$ and (b) $g_{N-Ow}(r)$ of membranes at $\lambda = 15$. (c) Cross-section snapshots of membranes at constant hydration, $\lambda = 15$, with dark gray particles representing the polymer chain, orange particles indicating Br^- ions and the cyan surface denoting the water region.

18304 | *J. Mater. Chem. A*, 2022, **10**, 18295–18307

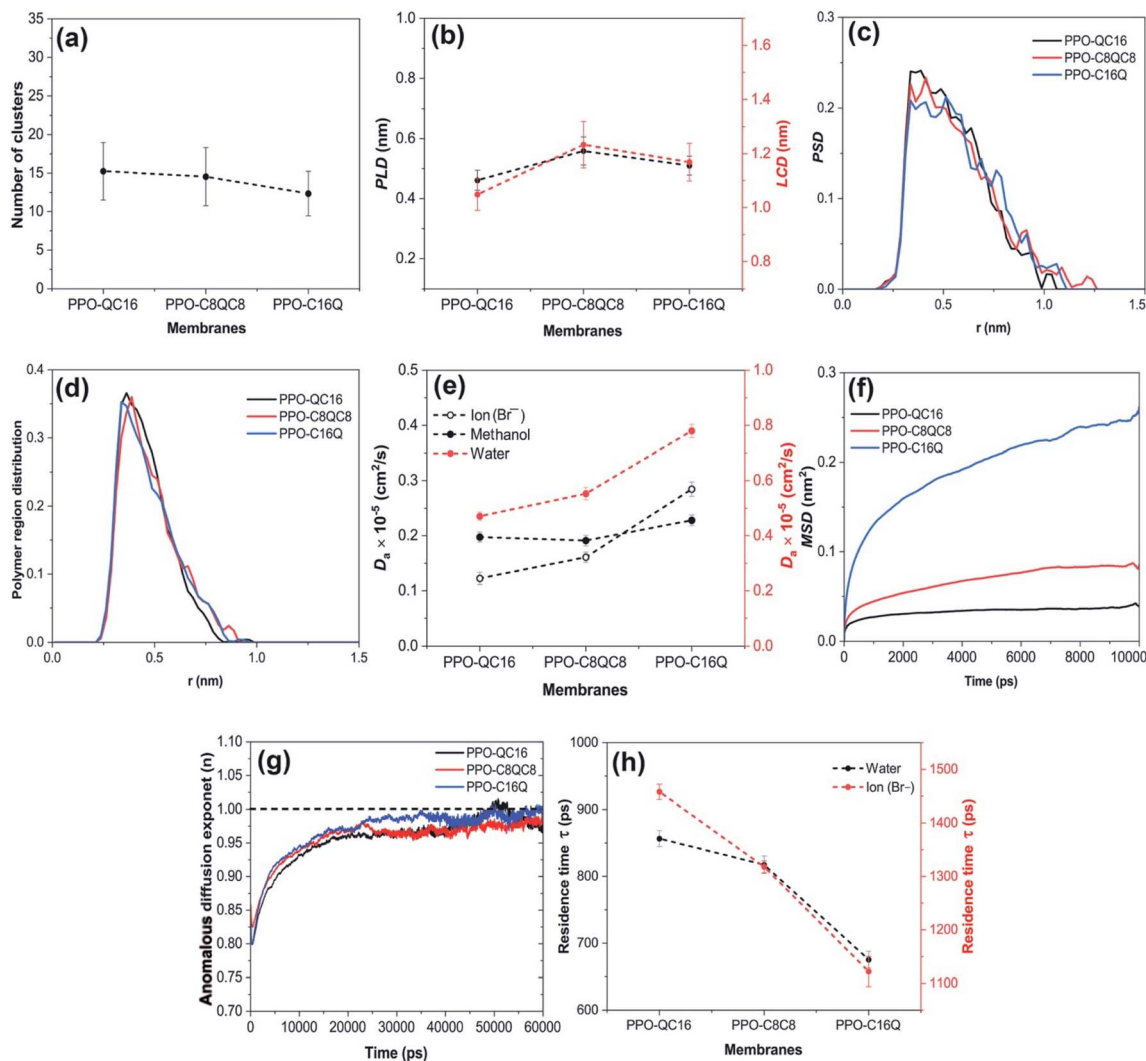This journal is © The Royal Society of Chemistry 2022

Fig. 5 (a) Number of clusters, (b) PLD and LCD, (c) water channel size distribution, PSD, (d) polymer region size distribution, PSD, (e) anomalous diffusion coefficient of Br^- ions and methanol (left) and water (right), (f) MSD of N^+, (g) anomalous diffusion exponent of water and (h) residence time of water (left) and Br^- ions (right) near N^+. Note that all membranes are at a constant hydration, $\lambda = 15$.

constant by moving QA towards the end of the side-chain in similar membranes. As shown in Fig. 5e, the diffusion coefficients of the ion and water show a considerable enhancement as the QA group is moved towards the end of the side-chain. This is totally in line with a recent study,[36] which reported enhanced ion mobility while the water channel width was found to be constant. Also, according to experimental studies,[72] an increase in QA mobility inside the water channel could enhance the anion transport in the membrane. Therefore, we calculated the MSD of N^+ in all membranes (Fig. 5f). Substantial growth is observed for MSD of N^+ in the PPO-C16Q membrane as compared to the others, which is consistent with the suggestions from similar simulations and experimental results indicating that longer alkyl spacer chains are more flexible and enhance QA mobility.[30,36] As the dynamics of N^+ increase, more water molecules become available to N^+, as also shown in Fig. 4b, enhancing water channel formation and increasing water and anion diffusion. Also, the anomalous diffusion

exponent result (see Fig. 5g) suggests that PPO-OC16 and PPO-C8QC8 membranes show very similar behavior. In contrast, for PPO-C16Q, water diffusion showed a closer-to-normal diffusion behavior in shorter simulation times. In addition, the residence time of water and anions near QA groups (Fig. 5h) confirms our previous finding. An increase in the mobility of N^+ decreases the residence time of the water/ion and facilitates their transport across the hydrophilic pathway. Thus, our study shows that moving the position of QA to the end of the alkyl side-chain enhances the anion transport but through a completely different mechanism. The hydrophilic pathway remains more or less similar, while the transport rate of the anion in the hydrophilic pathway is considerably enhanced as a result of the increased mobility of QA groups. In other words, our results suggest that while the morphologies of the membranes are similar, the longer spacer for QA groups results in a quicker hand-to-hand transport of anions due to the faster dynamics of

This journal is © The Royal Society of Chemistry 2022

J. Mater. Chem. A, 2022, **10**, 18295–18307 | **18305**

QA and shorter residence time of anions close to QA groups in the hydrophilic pathway.

We also computed the diffusion coefficient of methanol for the three systems and our models show that it remains almost constant (Fig. 5e) despite the significant enhancement in the QA mobility (Fig. 5f). This is probably attributed to the less polar nature of methanol as compared to water and the Br^- ion and accordingly weaker methanol–QA interaction so that the enhanced mobility of the pendant QA group does not affect the diffusion rate of methanol molecules in the channels. This is an interesting observation since it shows that one could enhance the ion conduction of these membranes by improving the QA group mobility while the methanol diffusion remains constant. This suggests that PPO membranes with pendant QA have a better ion/methanol selectivity as compared to PPO membranes without pendant QA.

4   Conclusion

In the current study, we conducted molecular dynamics simulations for hydrated PPO-QA-based AEMs to investigate the structure–diffusion relationship between them. The first aim of this work was to examine whether hydrophilic pathway morphology characteristics, i.e., PLD, LCD, and PSD, as described in ref. 11 for CEMs, are valid in describing the ion transport behavior of AEMs as well. We showed that the aforementioned characteristics are fairly able to describe the diffusion behavior of several PPO-QA membranes while the position of QA is fixed close to the polymer backbone. However, changing the position of QA on a long alkyl side-chain at constant hydration results in a significantly enhanced anion diffusion while the hydrophilic pathway morphological parameters remain almost constant. We showed that longer spacers for QA enhance the anion mobility in the water channels, thus affecting diffusion behavior by increasing the anion transport rate in the hydrophilic channels through enhanced QA dynamics but they have a negligible effect on the hydrophilic pathway morphology. Therefore, our findings suggest a two-stage strategy for designing polymer structures to be used as PPO-QA membranes: the polymer backbone in conjunction with the hydration level of the membranes determines the hydrophilic channel morphology while the QA spacers can tune the residence time and speed of anions in those channels. We also show that unlike polymer backbone modifications and increasing the hydration level (which increase ion and methanol diffusion more or less similarly), using a QA spacer does not increase the methanol diffusion rate despite the significant enhancement in ion mobility in the water channels. This is of great importance in the design of AEMs used for fuel cells in which the improvement in ion diffusion and controlling the methanol cross-over at the same time is a key requirement. It is worth emphasizing that our study puts forward a new methodology for assessing the effect of many material design strategies, like inclusion of nanoparticles, on the ion transport enhancement of IEMs to evaluate how they affect the hydrophilic channel morphology or ion transport rate in the channels.

Conflicts of interest

We have no conflict of interest to declare.

References

1 Y. Leng, G. Chen, A. J. Mendoza, T. B. Tighe, M. A. Hickner and C.-Y. Wang, *J. Am. Chem. Soc.*, 2012, **134**, 9054–9057.

2 M. A. Abdelkareem, K. Elsaid, T. Wilberforce, M. Kamil, E. T. Sayed and A. Olabi, *Sci. Total Environ.*, 2021, **752**, 141803.

3 W. Wang, Q. Luo, B. Li, X. Wei, L. Li and Z. Yang, *Adv. Funct. Mater.*, 2013, **23**, 970–986.

4 T. B. Ferriday and P. H. Middleton, *Int. J. Hydrogen Energy*, 2021, **46**, 18489–18510.

5 L. Li, J. Wang, L. Ma, L. Bai, A. Zhang, N. A. Qaisrani, X. Yan, F. Zhang and G. He, *ACS Sustainable Chem. Eng.*, 2021, **46**, 18489–18510.

6 R. Zhang, Y. Chen, D. Troya and L. A. Madsen, *Macromolecules*, 2020, **53**, 3296–3305.

7 J. Pan, S. Lu, Y. Li, A. Huang, L. Zhuang and J. Lu, *Adv. Funct. Mater.*, 2010, **20**, 312–319.

8 L. Hao, J. Liao, Y. Liu, H. Ruan, A. Sotto, B. Van der Bruggen and J. Shen, *Sep. Purif. Technol.*, 2019, **211**, 481–490.

9 M.-T. Lee, *J. Phys. Chem. B*, 2021, **125**, 2729–2740.

10 A. Barnett, J. Lu and V. Molinero, *J. Phys. Chem. C*, 2021, **125**, 27703–27713.

11 M. Rezayani, F. Sharif, R. R. Netz and H. Makki, *J. Membr. Sci.*, 2022, **654**, 120561.

12 L. Du, G. Zhang and S. Sun, *Automotive Innovation*, 2021, **4**, 131–143.

13 S. Lu, J. Pan, A. Huang, L. Zhuang and J. Lu, *Proc. Natl. Acad. Sci. U. S. A.*, 2008, **105**, 20611–20614.

14 A. D. Mohanty, Y.-B. Lee, L. Zhu, M. A. Hickner and C. Bae, *Macromolecules*, 2014, **47**, 1973–1980.

15 M. G. Marino, J. P. Melchior, A. Wohlfarth and K. D. Kreuer, *J. Membr. Sci.*, 2014, **464**, 61–71.

16 S. Chen, H. Wang, J. Zhang, S. Lu and Y. Xiang, *J. Membr. Sci.*, 2020, **605**, 118105.

17 C. Chen, Y.-L. S. Tse, G. E. Lindberg, C. Knight and G. A. Voth, *J. Am. Chem. Soc.*, 2016, **138**, 991–1000.

18 N. Chen and Y. M. Lee, *Prog. Polym. Sci.*, 2021, **113**, 101345.

19 M. Irfan, E. Bakangura, N. U. Afsar, M. M. Hossain, J. Ran and T. Xu, *J. Power Sources*, 2017, **355**, 171–180.

20 H. Lim, B. Lee, D. Yun, A. Z. Al Munsur, J. E. Chae, S. Y. Lee, H.-J. Kim, S. Y. Nam, C. H. Park and T.-H. Kim, *ACS Appl. Mater. Interfaces*, 2018, **10**, 41279–41292.

21 Z. Zhu, X. Luo and S. J. Paddison, *Solid State Ionics*, 2019, **340**, 115011.

22 J. Ran, L. Wu, Y. He, Z. Yang, Y. Wang, C. Jiang, L. Ge, E. Bakangura and T. Xu, *J. Membr. Sci.*, 2017, **522**, 267–291.

23 R. Gutru, Z. Turtayeva, F. Xu, G. Maranzana, B. Vigolo and A. Desforges, *Int. J. Hydrogen Energy*, 2020, **45**, 19642–19663.

24 Q. Liu, Z. Wang, A. Yu, J. Li, H. Shen, H. Wang, K. Yang and H. Zhang, *Int. J. Hydrogen Energy*, 2021, **46**, 24328–24338.

25 D. Dong, X. Wei, J. B. Hooper, H. Pan and D. Bedrov, *Phys. Chem. Chem. Phys.*, 2018, **20**, 19350–19362.

26 A. Ding, J. Zhou, X. Cheng, C. Shen and S. Gao, *J. Appl. Polym. Sci.*, 2021, **138**, 50201.

27 J. Ran, L. Wu, Y. Ru, M. Hu, L. Din and T. Xu, *Polym. Chem.*, 2015, **6**, 5809–5826.

28 S. A. Nunez, C. Capparelli and M. A. Hickner, *Chem. Mater.*, 2016, **28**, 2589–2598.

29 N. Li, Y. Leng, M. A. Hickner and C.-Y. Wang, *J. Am. Chem. Soc.*, 2013, **135**, 10124–10133.

30 H.-S. Dang and P. Jannasch, *Macromolecules*, 2015, **48**, 5742–5751.

31 M.-T. Lee, *J. Phys. Chem. C*, 2020, **124**, 4470–4482.

32 H.-S. Dang, E. A. Weiber and P. Jannasch, *J. Mater. Chem. A*, 2015, **3**, 5280–5284.

33 L. Li, J. Wang, M. Hussain, L. Ma, N. A. Qaisrani, S. Ma, L. Bai, X. Yan, X. Deng and G. He, *J. Membr. Sci.*, 2021, **624**, 119088.

34 X. Chu, J. Liu, S. Miao, L. Liu, Y. Huang, E. Tang, S. Liu, X. Xing and N. Li, *J. Membr. Sci.*, 2021, **625**, 119172.

35 H.-S. Dang and P. Jannasch, *J. Mater. Chem. A*, 2016, **4**, 17138–17153.

36 A. Barnett, J. Lu and V. Molinero, *J. Phys. Chem. C*, 2021, **125**, 27693–27702.

37 P.-G. De Gennes and P.-G. Gennes, *Scaling Concepts in Polymer Physics*, Cornell University Press, 1980.

38 W. Zhang, D. Dong, D. Bedrov and A. C. T. Van Duin, *J. Mater. Chem. A*, 2019, **7**, 5442–5452.

39 B. A. Paren, B. A. Thurston, A. Kanthawar, W. J. Neary, A. Kendrick, M. Maréchal, J. G. Kennemur, M. J. Stevens, A. L. Frischknecht and K. I. Winey, *Chem. Mater.*, 2021, **33**, 6041–6051.

40 A. L. Frischknecht, P. J. in't Veld, I. V Kolesnichenko, D. J. Arnot and T. N. Lambert, *ACS Appl. Polym. Mater.*, 2022, **4**, 2470–2480.

41 E. Lindahl, B. Hess and D. Van Der Spoel, *J. Mol. Model.*, 2001, **7**, 306–317.

42 W. L. Jorgensen and J. Tirado-Rives, *J. Am. Chem. Soc.*, 1988, **110**, 1657–1666.

43 P. Batys, Y. Zhang, J. L. Lutkenhaus and M. Sammalkorpi, *Macromolecules*, 2018, **51**, 8268–8277.

44 R. Zhang, X. Duan, M. Ding and T. Shi, *J. Phys. Chem. B*, 2018, **122**, 6656–6665.

45 B. A. Paren, B. A. Thurston, W. J. Neary, A. Kendrick, J. G. Kennemur, M. J. Stevens, A. L. Frischknecht and K. I. Winey, *Macromolecules*, 2020, **53**, 8960–8973.

46 A. D. Becke, *Phys. Rev. A: At., Mol., Opt. Phys.*, 1988, **38**, 3098.

47 P. J. Stephens, F. J. Devlin, C. F. Chabalowski and M. J. Frisch, *J. Phys. Chem.*, 1994, **98**, 11623–11627.

48 P. Mark and L. Nilsson, *J. Phys. Chem. A*, 2001, **105**, 9954–9960.

49 B. Hess, H. Bekker, H. J. C. Berendsen and J. G. E. M. Fraaije, *J. Comput. Chem.*, 1997, **18**, 1463–1472.

50 W. Humphrey, A. Dalke and K. Schulten, *J. Mol. Graphics*, 1996, **14**, 33–38.

51 T. E. Gartner III and A. Jayaraman, *Macromolecules*, 2019, **52**, 755–786.

52 L. Sarkisov, R. Bueno-Perez, M. Sutharson and D. Fairen-Jimenez, *Chem. Mater.*, 2020, **32**, 9849–9867.

53 S. Das, *Functional Fractional Calculus*, Springer, 2011, vol. 1.

54 L. Masaro and X. X. Zhu, *Prog. Polym. Sci.*, 1999, **24**, 731–775.

55 R. Metzler, J.-H. Jeon, A. G. Cherstvy and E. Barkai, *Phys. Chem. Chem. Phys.*, 2014, **16**, 24128–24164.

56 L. M. Thieu, L. Zhu, A. G. Korovich, M. A. Hickner and L. A. Madsen, *Macromolecules*, 2018, **52**, 24–35.

57 L. Zhu, J. Pan, Y. Wang, J. Han, L. Zhuang and M. A. Hickner, *Macromolecules*, 2016, **49**, 815–824.

58 F. I. Allen, L. R. Comolli, A. Kusoglu, M. A. Modestino, A. M. Minor and A. Z. Weber, *ACS Macro Lett.*, 2015, **4**, 1–5.

59 S. Kato, S. Yamaguchi, W. Yoshimune, Y. Matsuoka, A. Kato, Y. Nagai and T. Suzuki, *Electrochem. Commun.*, 2020, **111**, 106644.

60 F. Müller-Plathe, *J. Membr. Sci.*, 1998, **141**, 147–154.

61 K. B. Daly, J. B. Benziger, P. G. Debenedetti and A. Z. Panagiotopoulos, *J. Phys. Chem. B*, 2013, **117**, 12649–12660.

62 L. Zhu, T. J. Zimudzi, N. Li, J. Pan, B. Lin and M. A. Hickner, *Polym. Chem.*, 2016, **7**, 2464–2475.

63 E. Lin, X. You, R. M. Kriegel, R. D. Moffitt and R. C. Batra, *Comput. Mater. Sci.*, 2017, **138**, 448–461.

64 P. Batys, S. Kivistö, S. M. Lalwani, J. L. Lutkenhaus and M. Sammalkorpi, *Soft Matter*, 2019, **15**, 7823–7831.

65 Q. Berrod, S. Hanot, A. Guillermo, S. Mossa and S. Lyonnard, *Sci. Rep.*, 2017, **7**, 8326.

66 A. Sharifi-Viand, M. G. Mahjani and M. Jafarian, *J. Electroanal. Chem.*, 2012, **671**, 51–57.

67 F. Müller-Plathe, *J. Chem. Phys.*, 1998, **108**, 8252–8263.

68 F. Müller-Plathe, *Acta Polym.*, 1994, **45**, 259–293.

69 V. Molinero and W. A. Goddard III, *Phys. Rev. Lett.*, 2005, **95**, 45701.

70 Y. Lu, X. Pan, N. Li, Z. Hu and S. Chen, *Appl. Surf. Sci.*, 2020, **503**, 144071.

71 Y. Tang, D. Dubbeldam and S. Tanase, *ACS Appl. Mater. Interfaces*, 2019, **11**, 41383–41393.

72 M.-T. Lee, *J. Phys. Chem. C*, 2019, **123**, 10802–10815.

This journal is © The Royal Society of Chemistry 2022

J. Mater. Chem. A, 2022, **10**, 18295–18307 | 18307